# Boosting Visible Light Photocatalysis: $SnO_2$-Se Heterostructures

Stefania Mura , Pietro Rassu , Federico Fiori , Gabriele Masia , Sebastiano Garroni , Salvatore Marceddu , Ylenia Spissu , Luca Malfatti , Plinio Innocenzi *

Posted Date: 29 July 2025

doi: 10.20944/preprints202507.2363.v1

Keywords: tin oxide; selenium; photocatalysis; heterostructures

 doi:10.20944/preprints202507.2363.v1



*Article*

# Boosting Visible Light Photocatalysis: $SnO_2$-Se Heterostructures

**Stefania Mura [1], Pietro Rassu [1], Federico Fiori [1], Gabriele Masia [2], Sebastiano Garroni [2], Salvatore Marceddu [3], Ylenia Spissu [3], Luca Malfatti [1] and Plinio Innocenzi [1],***

[1] Laboratory of Materials Science and Nanotechnology (LMNT), CR-INSTM, Department of Biomedical Sciences, University of Sassari, Viale S. Pietro 43/B. 07100 Sassari. Italy

[2] Department of Chemistry, Physics, Mathematics and Natural Science, University of Sassari, Via Vienna 2, 07100 Sassari. Italy

[3] National Research Council of Italy (CNR), Institute of Sciences of Food Production (ISPA), Traversa La Crucca, 3 - Regione Baldinca, Li Punti. 07100 Sassari. Italy

* Correspondence: plinio@uniss.it

## Abstract

$SnO_2$–Se heterostructures have been synthesized via a facile hydrothermal approach to bridge the gap between ultraviolet-only and visible-only photocatalysis, and to enhance reactive oxygen species generation under visible illumination. Structural and morphological analyses using X-ray diffraction and scanning electron microscopy with energy dispersive spectroscopy have confirmed the coexistence of cassiterite $SnO_2$ particles intimately interfaced with trigonal selenium rods. Diffuse-reflectance spectroscopy revealed a long absorption tail extending into the 400–550 nm range. Under 450 nm sample illumination, the composite produced singlet oxygen in higher yields than either bare $SnO_2$ or Se, as evidenced by the indocyanine green assay. The system does not produce free radicals, as demonstrated by the terephthalic acid test; however, the addition of rhodamine B works as an effective sensitizer to generate hydroxyl radicals. Photodegradation tests using rhodamine B have shown that the $SnO_2$-Se heterostructure outperforms both its single components, Se and $SnO_2$, as a catalyst. The synergistic interplay underscores the potential of $SnO_2$–Se heterostructures in photochemical applications under visible light.

**Keywords:** tin oxide; selenium; photocatalysis; heterostructures

## Introduction

The growing need for photocatalytic materials active in the visible region of the spectrum has led to the exploration of several inorganic nanosystems for this purpose. Traditionally, materials such as $TiO_2$ (anatase)[1] and ZnO have dominated the field due to their high stability and low toxicity; however, they are only photoactive under UV irradiation because of their wide band gap (≈ 3.2 – 3.4 eV) [1]. To extend absorption to visible light, different strategies, including doping with heteroatoms (N, S, Fe-$TiO_2$) [2,3], dye sensitization [4], and the formation of heterostructures based on semiconductors with a smaller band gap [5], have been explored.

Among these approaches, mixed oxide heterostructures ($TiO_2$–$BiVO_4$ [6], ZnO–$Cu_2O$) [7,8] sulfide- or telluride-based semiconductors (CdS [9,10] $MoS_2$ [11] and CdTe [12]) and carbon-based compounds (g-$C_3N_4$ [13] and its mixtures with oxides [14,15]) have shown a good compromise between visible absorption (≤ 2.5 eV) and charge separation. However, despite these advantages, many materials exhibit distinct drawbacks. For instance, one key challenge is rapid recombination: photogenerated lifetimes often remain below the microsecond range, thereby limiting charge transfer efficiency [16]. Additionally, material stability can represent a critical issue. For instance, some sulfide [17] and telluride-based semiconductors [18] that are photoactive in the visible range tend to oxidize

 doi:10.20944/preprints202507.2363.v1



and release metal ions in aqueous environments [19]. Finally, while doping with transition metals or rare earths [20] improves visible absorption, it also raises the production costs and sustainability concerns [21].

$SnO_2$–Se heterostructures [22]represent an interesting combination between the wide-bandgap semiconducting nature of $SnO_2$ and the unique electrical and optical properties of selenium-based materials [23]. This heterostructure can enhance charge carrier separation, broaden light absorption, and tune electronic band alignments to improve performance across various devices [24]. Some examples have demonstrated the potential of $SnO_2$-Se heterostructures [25,26], such as photocatalytic degradation of methylene blue [27], [28] and high-sensitivity gas thermal sensing [29]; however, their properties and applications remain largely unexplored [30].

In this context, a $SnO_2$–Se heterostructure, obtained by a simple and scalable hydrothermal method [31], would offer several advantages. It can extend absorption up to 550 nm thanks to the Se component, without resorting to toxic doping. An effective separation of charge carriers through a well-defined band alignment is also an advantage: electrons can move from Se to $SnO_2$, while holes remain in Se, prolonging the lifetime of excited states.

The synthesis reported in the present work is straightforward: the material can be produced in a single step using a one-pot hydrothermal process at temperatures of 180°C or lower, employing only commonly used reagents. This combination of properties makes the $SnO_2$–Se system promising for applications in environmental decontamination and selective photocatalytic processes, offering a new perspective in the development of a new generation of catalytic nanosystems that are photoactivated by visible light and are based on the formation of *ad-hoc* designed heterostructures.

## Experimental

*Materials and methods*

Selenium powder 99.99%, sodium borohydride ($NaBH_4$), tin (II) chloride dihydrated ($SnCl_2 \cdot 2H_2O$), Rhodamine B, Terephthalic acid, Rhodamine B, Indocyanine green, NaOH 35%, were purchased from Sigma-Aldrich, USA. Milli Q water was used during the experiments. All reagents purchased were of analytical grade and used without further purification.

*Synthesis of $SnO_2$-Se composites*

The synthesis of the $SnO_2$-Se composite was carried out hydrothermally by adding the components in solution in different steps. Initially, an aqueous suspension of selenium and sodium borohydride ($NaBH_4$) was prepared. Selenium powder (Se) was used to form selenium anions by employing sodium borohydride as a reducing agent. In detail, 0.27 g of Se powder was mixed with 0.13 g of $NaBH_4$ in 35 mL of MQ water and stirred homogeneously for 1 hour at 70°C. The initial solution was brown. After 1 hour of stirring, 0.08 g $SnCl_2 \cdot 2H_2O$ were added and stirred for another hour. A dark green solution was initially obtained. As the reaction progresses, a black precipitate forms, accompanied by a yellow supernatant. Then, the solution was transferred to a 50 ml Teflon-lined autoclave for hydrothermal synthesis, heated at 180°C in an oven in air, and left to react for 24 hours. Finally, the solution was centrifuged at 9000 rpm for 20 minutes, and a black precipitate with a transparent supernatant was obtained, which was then discharged. The precipitate was finally put in an oven in air at 60°C to dry until a grey-black solid was obtained (Scheme 1). Reference $SnO_2$ was prepared by putting $SnCl_2 \cdot 2H_2O$ in an oven in air at 600°C for 2 h.

 doi:10.20944/preprints202507.2363.v1



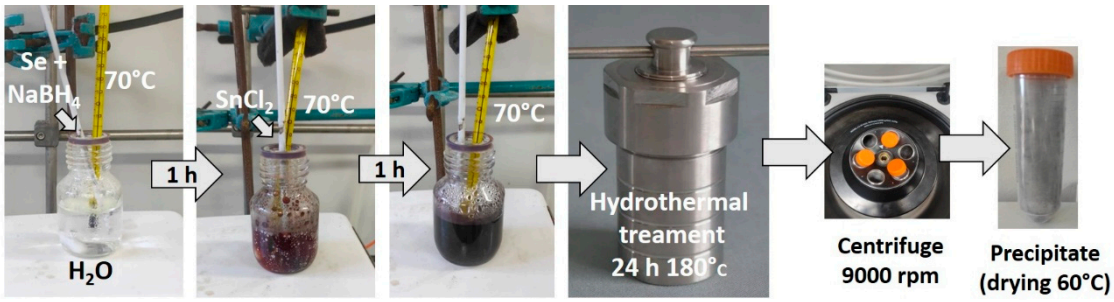


**Scheme 1.**

*Material Characterizations*

UV-Vis spectra were recorded on the powders pressed between two quartz slides of 1x1 cm in Diffuse-reflectance and converted in absorbance, using an Agilent Cary series UV-Vis-NIR spectrophotometer from 200 to 800 nm.

Photoluminescence emission spectra were recorded using a Spectrofluorometer (Horiba Jobin Yvon NanoLog) equipped with a 450 W xenon lamp as the excitation source. Fluorescence spectra of terephthalic acid were collected using a 2 nm slit, an excitation of 310 nm, and an emission of 315-600 nm.

Infrared spectra were obtained by using a Bruker Vertex 70 spectrophotometer in absorbance mode in the range of 4000–400 $cm^{-1}$, 4 $cm^{-1}$ resolution and 128 scans, using KBr pellets as substrates. The baseline was fitted by a concave rubber band correction with OPUS™ 7.0 software, and data were analysed by ORIGIN PRO™ software.

Raman spectra of $SnO_2$-Se were collected in the 65-1555 $cm^{-1}$ range with a 3-5 $cm^{-1}$ resolution using a Senterra confocal Raman microscope (Bruker, 785 nm laser, 100 mW power, and 50x objective), irradiating the powders deposited on a Si wafer.

The diffraction data were acquired in the 2θ range of 20–110°, employing a SMARTLAB diffractometer (Rigaku Corporation, Tokyo, Japan) equipped with a Cu $K_\alpha$ rotating anode source ($\lambda$ = 1.54178 Å, 40 kV, 100 mA), a graphite monochromator, and a scintillation counter. The sample was deposited on a silicon substrate, which was then placed on an amorphous glass slide employed for the measurements.

For SEM analysis the samples were coated with carbon or gold in an Agar Auto Carbon Coater B7367A. The acquisition images and element analysis and mappings by Energy Dispersive Spectroscopy (EDS) were conducted with a scanning electron microscope Zeiss EVO LS10 equipped with an Oxford INCAx-ACT EDS detector. The SEM was used in high vacuum mode, and the EDS analysis and element mappings were acquired using the AZtec software v 6.1 HF4.

*Indocyanine Green Assay*

Indocyanine green (ICG) was used to detect $^1O_2$ [32]. Irradiation was performed in a home-built reactor using a 75 W blue LED strip (5 m long, STRIP COB HC264075 15 W/MT 24 V IP20 Blue) with $\lambda$ = 450 nm. The strip was fixed to the surface of an aluminium can with glue and mounted on top of a magnetic stirrer. The temperature inside the photoreactor was kept at 25°C with the aid of multiple fans and a thermometer. The ICG stock solution was prepared by dissolving 1 mg ICG in 10 mL mQ water. From this stock solution, 100 µL was taken and diluted to 2 mL with mQ water and used as a reference sample. 2 mg of $SnO_2$-Se, Se, and $SnO_2$ powders were mixed with 100 µL ICG (stock) and diluted to 2 mL with mQ water. These two samples were irradiated with the previous LED at 450 nm and UV-Vis spectra were collected from 0 to 120 minutes. The same experiment was also carried out, adding 200 µL RhB to the previous solution with ICG and $SnO_2$-Se powder, and diluted to 2 mL with mQ water.

 doi:10.20944/preprints202507.2363.v1



*Terephthalic Acid Assay*

Terephthalic acid (TA) has been employed to detect hydroxyl radicals ($OH^{\cdot}$) for its property of reacting with these radicals to form 2-hydroxyterephthalic acid (HTA), which is fluorescent [33]. The measurement of this fluorescence enables the quantification of OH radical concentration. A stock solution was prepared by dissolving 20 mg TA / 50 mL of mQ water. To facilitate the dissolution of TA, 6.25 µL NaOH 35% was added. 1 mL of this solution was added to 2 mg of powders ($SnO_2$-Se, $SnO_2$, or Se), and 2 mL of water was added, for a total of 3 mL of solution. For the experiment with the dye, 1 mL of TA solution was added to 2 mg of $SnO_2$-Se powder and 200 µL of RhB (0.1 mg $mL^{-1}$), resulting in a total solution volume of 3 mL in water. As a reference, 200 µL RhB was dissolved in 3 mL of water, and for TA measurement, 1 mL TA was dissolved in 3 mL of water. PL spectra were measured at t = 0 ($t_0$) and after irradiation with a blue LED for 30 and 60 minutes.

*Photodegradation Experiments of Rhodamine B*

The samples were prepared by dissolving 200 µL of RhB (0.1 mg $mL^{-1}$) in 2 mL of mQ water as a standard. The test samples were prepared as before, but with the addition of 2 mg of $SnO_2$-Se, $SnO_2$ and Se powder. The UV-Vis spectra were collected at $t_0$ and after irradiation with LEDs at 30-minute intervals for a total of 120 minutes. For the experiment, the blue LED was operated at its maximum irradiation power (100%, 75 W), and the cuvette was placed 10 cm from the reactor wall.

## Results and Discussion

The formation of a nanocomposite, such as $SnO_2$-Se, was initially studied using X-ray diffraction analysis to investigate the crystalline phases formed in the heterostructured material (Figure 1).

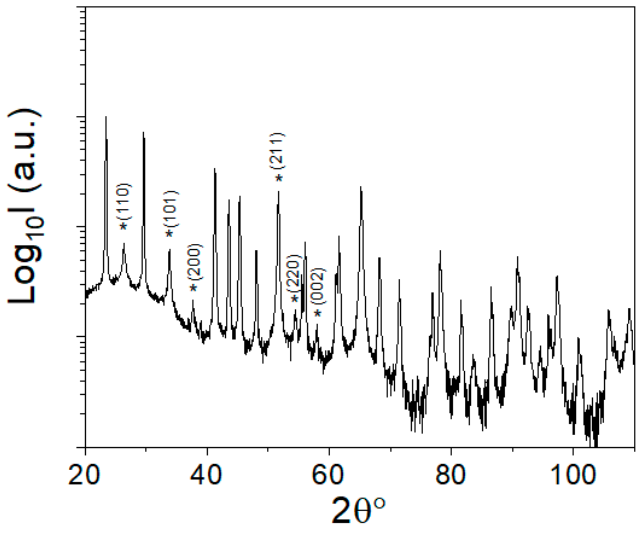


**Figure 1.** XRD patterns of $SnO_2$-Se powder. $SnO_2$ cassiterite tetragonal rutile structure (indicated with an asterisk) and trigonal Se are detected.

The analysis of the $SnO_2$-Se powders shows the presence of two distinct crystalline phases, $SnO_2$ cassiterite tetragonal rutile structure (JCPDS card n. 41-1445) and trigonal Se (JSPDS card n. 06-0362), the thermodynamically stable form of crystalline Se at room temperature. Interestingly, the formation of two phases is in contrast with what was observed by Reddy et al. [33], who obtained a single $SnSe_2$ phase using a similar synthesis method. $SnSe_2$ is a layered dichalcogenide with a hexagonal structure [34] with the main reflection peaks at ~14.4° (001), $I_{100}$, and ~29° (002) $I_{60\text{-}70}$. In our case, however, we

 doi:10.20944/preprints202507.2363.v1



have not employed an inert atmosphere, and a Se-$SnO_2$ structure, rather than $SnSe_2$, has formed because the atmosphere contains oxygen.

The XRD data well support the hypothesis of the formation of a Se-$SnO_2$ nanostructured composite, while the presence of $SnSe_2$ can be ruled out because no corresponding diffraction signals have been detected. The average crystallite dimensions have been calculated by the Rietveld method $SnO_2$ = 29.0 and Se = 14.9 nm.

The XRD data indicate the formation of heterostructures composed of crystalline Se and $SnO_2$. To get a direct insight into the material morphology, we have analysed the samples by SEM and EDS (**Figure 2**).

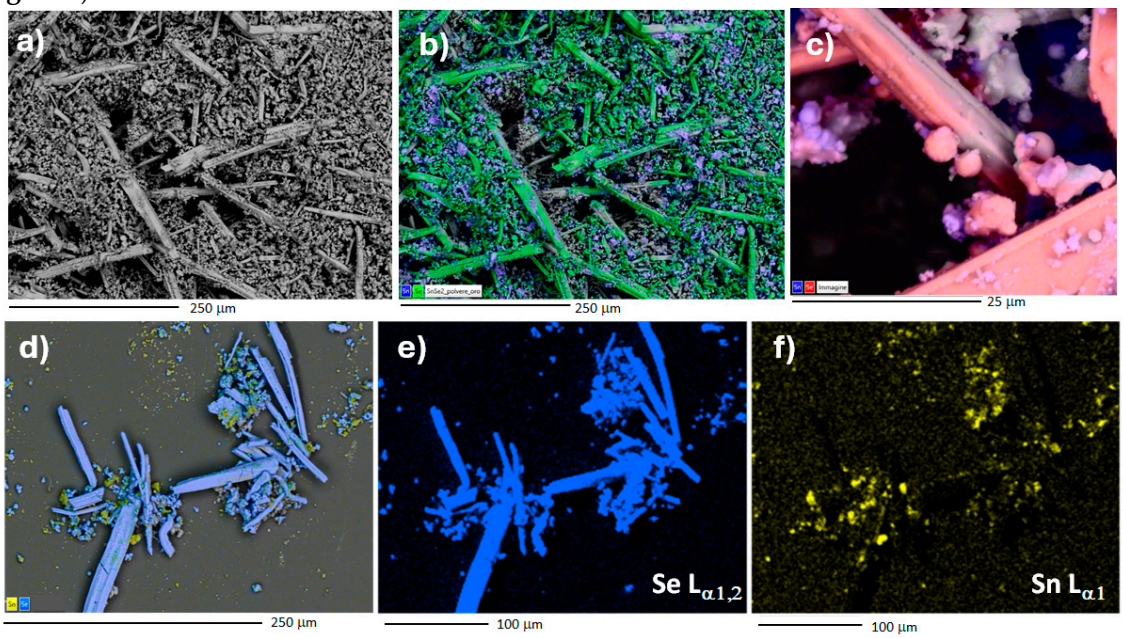


**Figure 2.** a) SEM image of the $SnO_2$-Se heterostructures. b) Energy Dispersive Spectroscopy (EDS) map of image in a, showing the distribution of Sn (in violet) and Se (in green) elements. c) SEM image with the detail of the composite and the distribution of Sn (blue) and Se (red) elements. d) SEM image showing the formation of two distinct structures, rod-like crystals and spherical particles. e) Distribution of Se in image d and f) distribution of Sn in image d.

The SEM and EDS analysis show that the $SnO_2$-Se is formed by two well-distinct structures with defined shapes (Figure 2a). The first one consists of elongated rods measuring a few hundred microns. Together with these rods, spherical particles of sub-micron size are also observed. EDS analysis has enabled the distinction between the two structures: the more elongated ones are composed of selenium crystals, while the particles are composed of tin dioxide (Figures 2b-f).

To investigate the structure of the nanostructured composite, we have also employed Raman and FTIR spectroscopy as supporting evidence. Figure 3a shows the Raman spectrum of the $SnO_2$-Se sample in the 100 – 500 $cm^{-1}$ interval; no signals have been observed beyond this range. The spectrum exhibits two intense bands peaking at 141 and 234 $cm^{-1}$. The first band corresponds to the transverse optical phonon mode (E mode) [35]. The second band, observed at higher wavenumbers, is characteristic of trigonal selenium (t-Se) and is assigned to the stretching vibration of helical selenium chains ($A_1$ mode). The weak band around 459 $cm^{-1}$ is, instead, attributed to the first overtone of t-Se $A_1$ mode [36].

 doi:10.20944/preprints202507.2363.v1



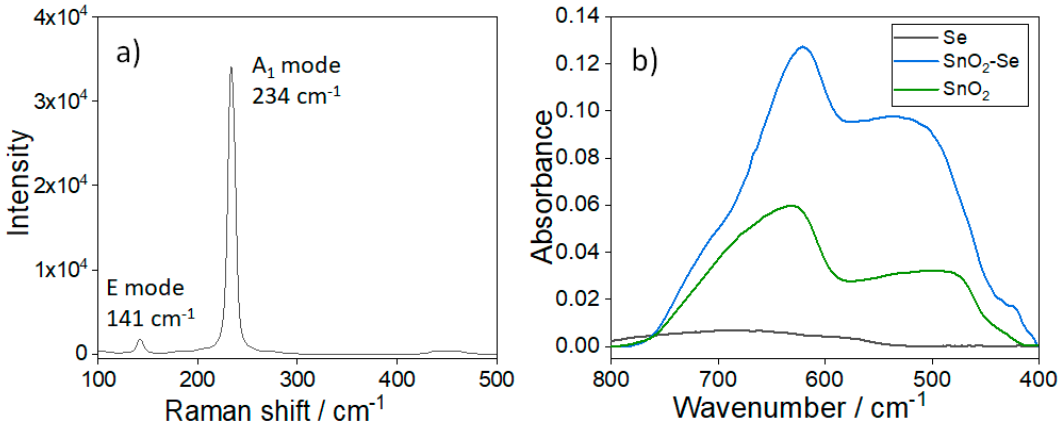


**Figure 3.** a) Raman spectra and b) FTIR absorption spectra of the $SnO_2$-Se heterostructure. The infrared spectra of Se and $SnO_2$ are reported as a reference.

We have used infrared spectroscopy as a complementary technique to Raman spectroscopy. Figure 3b shows the FTIR absorption spectra in the 800-400 $cm^{-1}$ range of the as-synthesized $SnO_2$-Se powder with the Se and $SnO_2$ used as a reference (Full spectra are reported in **SI1**). The $SnO_2$-Se infrared spectrum shows two broad absorption bands peaking at 620 and 534 $cm^{-1}$ [37,38]. The $SnO_2$ sample shows a similar spectrum, while Se does not absorb infrared light in the same range. The FTIR spectrum of cassiterite $SnO_2$ is dominated by a broad $E_u$-derived antisymmetric stretch peaking at 629 $cm^{-1}$ and a weaker $A_{2u}$ bending around ~547–610 $cm^{-1}$. The same features are observed in the $SnO_2$-Se sample at 620 and 534 $cm^{-1}$, confirming the formation of the $SnO_2$ phase. The $SnO_2$-Se spectra suggest the presence of a nanosized fraction of $SnO_2$ particles. In fact, as the particle size decreases, the lower-frequency component (~534 $cm^{-1}$) grows in relative intensity, and the high-frequency stretch peak (~620 $cm^{-1}$) can shift slightly toward lower wavenumbers (red-shift) due to phonon confinement and increased lattice strain.

Figure 4 shows the diffuse reflectance UV-Vis absorption spectra of Se-$SnO_2$, and reference Se and $SnO_2$. The Se spectrum is characterized by an absorption onset around 690 nm, corresponding to an indirect band gap of 1.71 eV (calculated by Tauc plot). $SnO_2$, on the other hand, is a direct band gap semiconductor and has a sharp absorption edge that typically starts around 330–350 nm, corresponding to a band gap of 3.73 eV. Interestingly, in the Se-$SnO_2$ composite a longer tail extending from Se band edge up the $SnO_2$ visible region, due to interfacial and defect states, is observed [39]. Increasing the absorption toward longer wavelengths enhances sensitivity in the red region.

 doi:10.20944/preprints202507.2363.v1



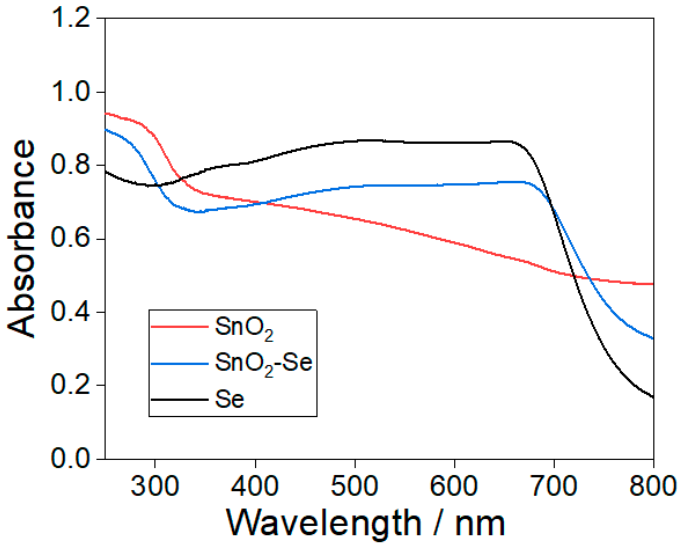


**Figure 4.** Diffuse reflectance UV-Vis absorption spectra of $SnO_2$, Se and $SnO_2$-Se.

To assess the production of radicals or ROS by $SnO_2$-Se when illuminated by visible light, two tests have been performed. The first one is the green indocyanine (IGC) assay (Figure 5). ICG, which has an absorption peak around 780 nm in aqueous solution, is stable under visible-light irradiation in the absence of $^1O_2$, but undergoes oxidative cleavage of its polymethine chain in the presence of singlet oxygen [40]. The net effect is a decrease in the ICG absorbance at ~780 nm that is proportional to the cumulative amount of $^1O_2$ generated in the system. [41]

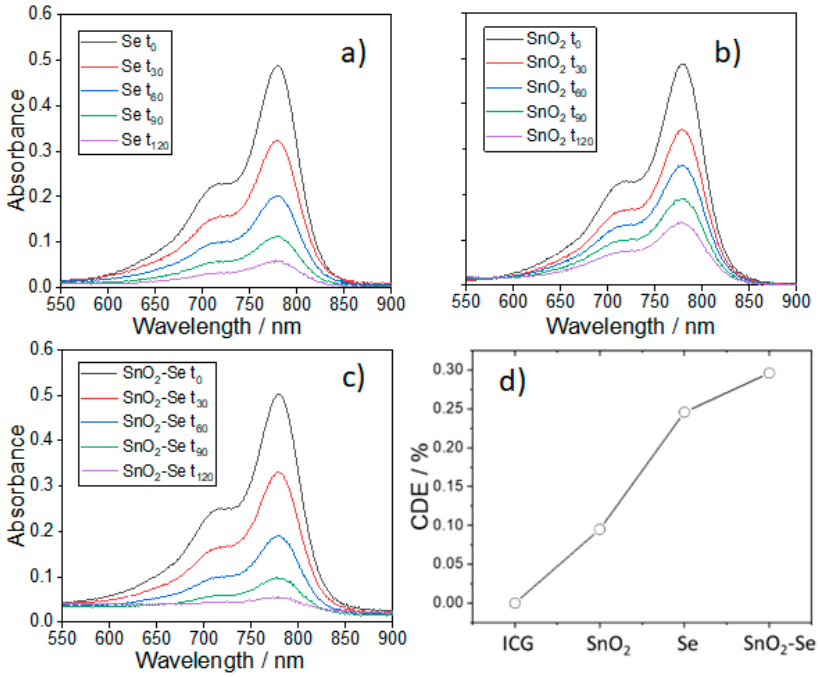


**Figure 5.** ROS emission test by indocyanine (IGC) assay. Optical absorption spectra of an aqueous solution of indocyanine and: a) Se; b) $SnO_2$ and $SnO_2$-Se samples upon exposition to blue light ($\lambda$ = 450 nm) for different times, up to 120 min ($t_{120}$). d) Comparative degradation efficiency (CDE).

Figure 5a, b, and c show the effect of the exposure to blue light ($\lambda$ = 450 nm) of an aqueous solution containing ICG, the reference samples Se and $SnO_2$, and the $SnO_2$-Se heterostructure. The

 doi:10.20944/preprints202507.2363.v1



test shows a time-dependent reduction in the absorbance of the 780 nm band for all samples, indicating the formation of singlet oxygen upon exposure to visible light [42]. Figure 5d displays the comparative degradation efficiency (CDE) calculated by the following formula [43]:

$$CDE\ (\%) = 1 - [A_{0\ (ICG)} - A_{120\ (ICG)}] / [A_{0\ (sample)} - A_{120\ (sample)}] \qquad (2)$$

The ICG experiment indicates that while both $SnO_2$ and Se are still capable of generating singlet oxygen upon illumination with blue light, the $SnO_2$-Se heterostructure enhances the emission.

The other assay is based on terephthalic acid (TA) [44], which is a selective chemical probe for hydroxyl radicals (•OH) (Figure 6). In aqueous solution, TA itself is essentially non-absorbing and non-fluorescent in the near-UV/visible region. When •OH attacks TA, it hydroxylates the aromatic ring to give 2-hydroxyterephthalic acid (2-HTPA), which exhibits a characteristic fluorescence at ≈ 425 nm that can be used for the test. The test has also been performed using Se and $SnO_2$ samples as references, and no formation of radicals has been observed. Exposure to visible light (450 nm) does not produce any hydroxyl radicals, as no significant changes in the fluorescence band at 425 nm are detected. The two tests, ICG and TA assays, demonstrate that the $SnO_2$-Se heterostructure, upon excitation by visible light, generates singlet oxygen but not hydroxyl radicals.

Interestingly, the same test repeated by adding RhB has shown different results. In Se and $SnO_2$ samples, no differences have been observed, while the $SnO_2$-Se sample shows a significant change. The hydroxyl radical (•OH) detection test shows, in fact, an increased fluorescence intensity of the band assigned to the formation of 2-HTPA (around 425 nm), indicating an enhanced production of hydroxyl radical (Figure 6d).

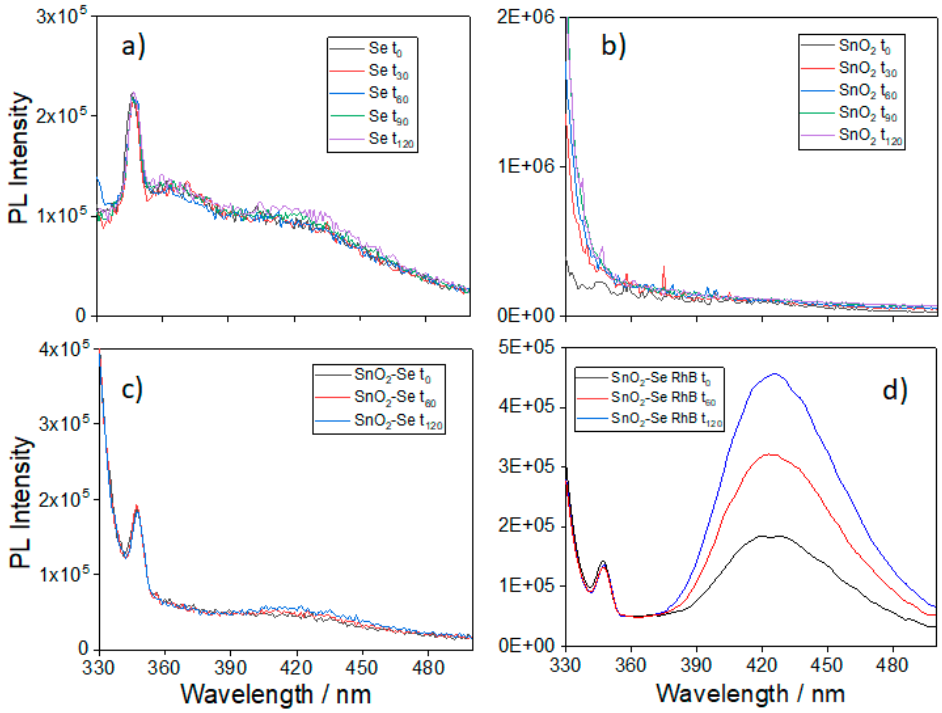


**Figure 6.** Photoluminescence emission spectra of terephthalic acid measured in solutions containing the different samples and exposed to 450 nm radiation for different times (from 0 ($t_0$) to 120 ($t_{120}$) minutes). a) Se; b) $SnO_2$; c) $SnO_2$-Se and d) $SnO_2$-Se powder with the addition of RhB.

In the terephthalic acid assay, only the •OH (hydroxyl) radicals generated under illumination are detected. Neither bare Se nor bare $SnO_2$ produces a measurable •OH signal because $SnO_2$ is a wide-band-gap semiconductor (≈ 3.6 eV) that mainly absorbs UV light (< 350 nm). Under typical visible-light or near-UV illumination used in many radical tests, $SnO_2$ is not photoexcited enough to drive water oxidation to •OH. On the other hand, crystalline Se absorbs more in the visible spectrum; however, as a zero-band-gap or very small-band-gap "semimetal," photogenerated carriers

 doi:10.20944/preprints202507.2363.v1



recombine very quickly. Crystalline selenium efficiently produces singlet oxygen (see **Figure 5a**) because the absorbed photon energy is almost exclusively involved in the generation of triplet excitons. These in turn transfer energy to $O_2$ to form singlet oxygen with high quantum yield. In absence of a photosensitiser, the energy transfer mechanism to convert $O_2$ into $^1O_2$ is much more efficient than the multistep redox sequences required to produce $^{\bullet}OH$ species. Finally, in crystalline selenium there is no built-in electric field or heterojunction to pull electrons and holes apart, so almost no oxidative chemistry ($^{\bullet}OH$ formation) succeeds before recombination. In both bare materials, any electrons and holes that form upon light absorption recombine on a sub-nanosecond timescale, while an efficient spatial separation of charges is necessary to allow holes to oxidize surface water ($H_2O \rightarrow {}^{\bullet}OH + H^+ + e^-$).

On the other hand, Rhodamine B strongly absorbs visible light, exhibiting a broad absorption band peaking around 550 nm. When the $SnO_2$–Se–RhB system is irradiated with visible light, RhB is excited (RhB → RhB*), and can inject an electron into the Se valence or conduction band (depending on alignment), which then cascades into $SnO_2$ [45]. The extra injected electron leaves behind an $RhB^{+\bullet}$ radical cation; the photogenerated hole on RhB (or in Se) is highly oxidizing and can oxidize surface $H_2O$ or $OH^-$ to $^{\bullet}OH$. Meanwhile, the transferred electron in $SnO_2$ can reduce $O_2$ to superoxide, which may further form $^{\bullet}OH$ via secondary pathways. The $SnO_2$–Se + RhB system benefits from dye sensitization, efficient heterojunction charge separation, and appropriate surface reaction sites, enabling the holes (and/or superoxide intermediates) to oxidize water into detectable $^{\bullet}OH$ radicals [46].

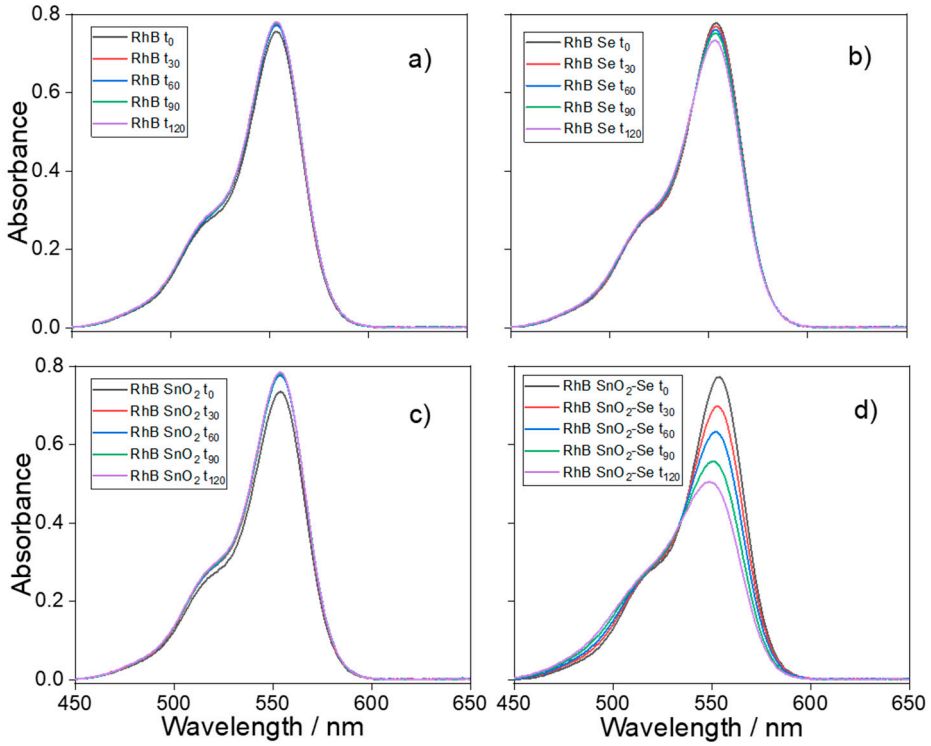


**Figure 7.** UV-Vis absorption spectra of RhB illuminated by blue light (450 nm) for different times, up to 120 min ($t_{120}$). a) RhB; b) RhB + Se; c) RhB + $SnO_2$ and d) RhB + $SnO_2$-Se.

We then performed another experiment using only RhB as the test molecule. RhB does not absorb light under 450 nm, and under illumination by blue light, it does not degrade (Figure 7a). The addition of Se or $SnO_2$ to the aqueous solution produces only a slight reduction in the absorption maxima. If, instead, $SnO_2$-Se is added to the RhB solution, a 36% absorbance reduction is observed. The result confirms that the $SnO_2$-Se heterostructure plays a synergistic role. Under 450 nm illumination, only materials whose absorption edge extends into the blue can be photoexcited, and

 doi:10.20944/preprints202507.2363.v1



only systems that can both separate those photo-carriers and channel them into redox chemistry will drive dye degradation. This explains why the $SnO_2$–Se heterostructure works well when either component alone fails. The $SnO_2$–Se heterostructure combines visible-light harvesting, efficient charge separation, parallel ROS-forming pathways, and dye sensitization into a single system, enabling rapid RhB degradation under 450 nm light that neither bare $SnO_2$ nor bare Se can achieve. The Rhodamine B test is also an indication of the photodegradation capability of the $SnO_2$-Se heterostructure.

## Conclusions

In this study, we have demonstrated that $SnO_2$–Se heterostructures synthesized via a simple one-pot hydrothermal method exhibit enhanced visible-light photocatalytic performance compared to their individual components. Under 450 nm irradiation, the composite generates singlet oxygen ($^1O_2$) more efficiently than the individual components, as confirmed by the indocyanine green assay. Photodegradation of rhodamine B under visible light outpaces that of bare $SnO_2$ and Se. The absence of toxic dopants or noble metals, combined with mild hydrothermal conditions, underlines the scalability and eco-friendliness of $SnO_2$-Se composites relative to existing visible light photocatalysts. Future work should focus on in-depth spectroscopic studies (e.g., time-resolved photoluminescence, transient absorption) to directly quantify interfacial charge dynamics. Moreover, extending this heterostructure concept to other chalcogen–oxide combinations is a feasible route for visible-light-active photocatalysts in environmental and synthetic photochemistry.

**Author Contributions:** Stefania Mura: conceptualization, data curation, formal analysis, investigation, methodology, software, validation, visualization, writing original draft, writing review and editing Pietro Rassu: data curation, formal analysis, contact angle measurements and contribution to graphical abstract Federico Fiori: Data and graph curation, Indocyanine test Salvatore Marceddu: SEM measurements Ylenia Spissu: elemental analysis and SEM Gabriele Masia: XRD measurements Sebastiano Garroni: XRD analysis Luca Malfatti: writing review and editing Plinio Innocenzi: conceptualization, data curation, funding acquisition, investigation, project administration, resources, supervision, validation, visualization, writing original draft, writing review and editing

**Conflicts of Interest:** The authors declare no conflicts of interest.

**Data Availability:** The data supporting this article have been included as part of the Supplementary Information

**Funding:** We acknowledge the PRIN projects n. 2022LZWKAJ "Engineered nano- heterostructures for a new generation of titania photocatalytic films (ENTI)" and n. P2022JRB2Y " Engineered robust-composite photoelectrodes with enhanced durability and solar-to chemical energy conversion" for their funding. We acknowledge financial support under the National Recovery and Resilience Plan (NRRP), Mission 4, Component 2, Investment 1.1, Call for tender No. 1409 published on 14.9.2022 by the Italian Ministry of University and Research (MUR), funded by the European Union – Next Generation EU– Project Title "Engineered robust-composite photoelectrodes with enhanced durability and solar-to chemical energy conversion" N. P2022JRB2Y – CUP J53D23015880001- Grant Assignment Decree No. 966 adopted on 30/06/2023 by the Italian Ministry of Ministry of University and Research (MUR).

**Acknowledgment:** We thank Dr. Luigi Stagi for the scientific and technical support for AFM and XRD measurements.

## References

1. Fujishima, A.; Honda, K. Electrochemical photolysis of water at a semiconductor electrode. *Nature* **1972**, 238, 37–38. https://doi.org/10.1038/238037a0
2. Asahi, R.; Morikawa, T.; Ohwaki, T.; Aoki, K.; Taga, Y. Visible-light photocatalysis in nitrogen-doped titanium oxides. *Science* **2001**, 293, 269–271. https://doi.org/10.1126/science.1061051

 doi:10.20944/preprints202507.2363.v1




3. S. Mura; G. Greppi; P. Innocenzi; M. Piccinini; C. Figus; M.L., Marongiu; C. Guo; J. Irudayaraj; Nanostructured thin films as surface-enhanced Raman scattering substrates. *J. Raman Spectrosc.* **2013**, 44, 35-40. DOI: 10.1002/jrs.4151
4. O◙Regan, B.; Grätzel, M. A low-cost, high-efficiency solar cell based on dye-sensitized colloidal $TiO_2$ films. *Nature* **1991**, 353, 737–740. https://doi.org/10.1038/353737a0
5. Chen, X.; Mao, S.S. Titanium dioxide nanomaterials: Synthesis, properties, modifications, and applications. *Chem. Rev.* **2007**, 107, 2891–2959. https://doi.org/10.1021/cr0500535
6. Y., R.; Liu, C., J.; He, R., K.; Li, X.; Xu, Y.-H. $BiVO_4/TiO_2$ heterojunction with enhanced photocatalytic activities and photoelectrochemical performances under visible light illumination. *Mater. Res. Bull.* **2019**, *117*, 35–40. https://doi.org/10.1016/j.materresbull.2019.04.032.
7. Özdal, T.; Kavak, H. Fabrication and characterization of ZnO/$Cu_2O$ heterostructures for solar cells applications. *Superlattices Microstruct.* **2020**, *146*, 106679. https://doi.org/10.1016/j.spmi.2020.106679.
8. Abdi, F.F.; van de Krol, R. Nature and light dependence of bulk recombination in Co–Pi–catalyzed $BiVO_4$ photoanodes. *J. Phys. Chem. C* **2012**, 116, 9398–9404. https://doi.org/10.1021/jp301774c
9. Cheng, L.; Quanjun, X.; Liao, Y.; Zhang, H. CdS-Based photocatalysts. *Energy Environ. Sci.* **2018**, *11*, 1754–1765. https://doi.org/10.1039/C7EE03640J.
10. Akhtar, N.; Choi, C.; Ateeq, M.; Fazil, P.; Shah, N. S.; Khan, J. A.; Al-Sehemi, A. G.; Zada, A.; Shah, M. I. A.; Ikram, R.; Han, C. Visible light active CdS/CuO nanocomposites for photocatalytic degradation of ciprofloxacin, H2 production and antimicrobial activity. *Chem. Eng. J.* **2025**, *507*, 160336. https://doi.org/10.1016/j.cej.2025.160336.
11. Rahman, A.; Jennings, J. R.; Tan, A. L.; Khan, M. M. Molybdenum disulfide-based nanomaterials for visible-light-induced photocatalysis. *ACS Omega* **2022**, *7*, 22089–22110. https://doi.org/10.1021/acsomega.2c01314.
12. Muslih, E. Y.; Munir, B.; Khan, M. M. Advances in chalcogenides and chalcogenide-based nanomaterials such as sulfides, selenides, and tellurides. *Micro and Nano Technologies: Chalcogenide-Based Nanomaterials as Photocatalysts*. **2021**; 7–31. https://doi.org/10.1016/B978-0-12-820498-6.00002-0.
13. Yang, Y.; Chen, J.; Mao, Z.; An, N.; Wang, D.; Fahlman, B. D. Ultrathin g-$C_3N_4$ nanosheets with an extended visible-light-responsive range for significant enhancement of photocatalysis. *RSC Adv.* **2017**, *7*, 2333. https://doi.org/10.1039/c6ra26172h.
14. Alaya, Y.; Chouchene, B.; Medjahdi, G.; Balan, L.; Bouguila, N.; et al. Heterostructured S-TiO2/g-$C_3N_4$ photocatalysts with high visible light photocatalytic activity. *Catalysts* **2024**, *14*, 226. https://doi.org/10.3390/catal14040226.
15. Wang, Y.; Wang, X.; Antonietti, M. Polymeric graphitic carbon nitride as a heterogeneous organocatalyst: What is the actual active structure? *Angew. Chem.* **2012**, 51, 68–89. https://doi.org/10.1002/anie.201101182
16. Kudo, A.; Miseki, Y. Heterogeneous photocatalyst materials for water splitting. *Chem. Soc. Rev.* **2009**, 38, 253–278. https://doi.org/10.1039/B800489G
17. Kim, J.H., Kim, M., Kim, SJ. et al. Understanding the electrochemical processes of $SeS_2$ positive electrodes for developing high-performance non-aqueous lithium sulfur batteries. *Nat. Commun.* **2024**, 15, 7669. https://doi.org/10.1038/s41467-024-51647-5
18. Su, MY., Li, XY. & Zhang, JT. Telluride semiconductor nanocrystals: progress on their liquid-phase synthesis and applications. *Rare Met.* **2022**, 41, 2527–2551. https://doi.org/10.1007/s12598-022-01980-9
19. Dutta, D.P.; Tyagi, A.K.; Raj, B. $MoS_2$ as a new efficient visible-light driven photocatalyst. *Catal. Today* **2011**, 161, 276–280. https://doi.org/10.1016/j.cattod.2010.10.057
20. Hu, H.; Zhang, W. Synthesis and properties of transition metals and rare-earth metals doped ZnS nanoparticles. *Opt. Mater.* **2006**, *28*, 536–550. https://doi.org/10.1016/j.optmat.2005.03.015.
21. Liu, G.; Wang, L.; Yang, H.G.; Cheng, H.-M.; Lu, G.Q. Titanium dioxide crystals with tailored facets. *Chem. Rev.* **2014**, 114, 9559–9612. https://doi.org/10.1021/cr400621z
22. Li, X.; Ge, W.; Wang, P.; Han, K.; Zhao, H.; Zhang, Q.; Diwu, H.; Liu, Z. Near-infrared enhanced SnO2/SnSe2 heterostructures for room-temperature NO2 detection: Experiments and DFT calculations. *Sens. Actuators B Chem.* **2023**, *397*, 134643. https://doi.org/10.1016/j.snb.2023.134643.
23. Huang, Y.; Su, E.; Ren, J.; Qu, X. The recent biological applications of selenium-based nanomaterials. *Nano Today* **2021**, *38*, 101205. https://doi.org/10.1016/j.nantod.2021.101205.

 doi:10.20944/preprints202507.2363.v1




24. Li, W.; Zhang, X.; Qiu, Y.; Zhou, M.; Huang, Y. Selenium-modified $SnO_2$ nanocomposites for improved photocatalytic activity. *J. Mater. Sci. Technol*. **2021**, 74, 103–110. https://doi.org/10.1016/j.jmst.2020.09.066
25. Shen, A.; Shi, Z.; Zhang, W.; Zhai, Y.; Feng, Y.; Gong, W.; Xu, P.; Li, Q. Constructing $SnO_2$/$SnSe_2$ heterostructures anchored on reduced graphene oxide for advanced lithium-ion batteries. *J. Colloid Interface Sci.* **2025**, 700, 138460. https://doi.org/10.1016/j.jcis.2025.138460
26. Paolucci, V.; D'Olimpio, G.; Kuo, C. N.; Lue, C. S.; Boukhvalov, D. W.; Cantalini, C.; Politano, A. Self-assembled $SnO_2$/$SnSe_2$ heterostructures: a suitable platform for ultrasensitive $NO_2$ and $H_2S$ sensing. *ACS Appl. Mater. Interfaces* **2020**, 12, 34362–34369. https://doi.org/10.1021/acsami.0c07901
27. Alamo-Nole, L.; Bailon-Ruiz, S. J. Photocatalytic degradation of methylene blue by surface-modified $SnO_2$/Se-doped QDs. *Micro* **2024**, 4, 721–733. https://doi.org/10.3390/micro4040044
28. Zhou, Y.; Zhang, C.; Wang, Y.; Liang, Y. Photocatalytic performance of $SnO_2$/Se heterojunctions for dye degradation under visible light. *Appl. Surf. Sci.* **2020**, *506*, 144923. https://doi.org/10.1016/j.apsusc.2019.144923
29. Park, J. Y.; Lee, C. Y.; Choi, J. Y.; Kim, D. H. $SnO_2$–Se composites for selective gas sensing applications at low temperatures. *Sens. Actuators B Chem.* **2019**, *283*, 100–107. https://doi.org/10.1016/j.snb.2018.12.025
30. Yu, J.; Low, J.; Xiao, W.; Zhou, P.; Jaroniec, M. Enhanced photocatalytic $CO_2$ reduction by $TiO_2$/graphene composites: a review. *J. Am. Chem. Soc.* **2014**, *136*, 8839–8842. https://doi.org/10.1021/ja5025287
31. Swamy Reddy, K.; Veeralingam, S.; Borse, P. H.; Badhulika, S. A flexible, rapid response, hybrid inorganic–organic $SnSe_2$–PEDOT:PSS bulk heterojunction based high performance broadband photodetector. *Mater. Chem. Front*. **2022**, 6, 341–351. https://doi.org/10.1039/D1QM01232.
32. Engel, E.; Schraml, R.; Maisch, T.; Kobuch, K.; König, B.; Szeimies, R.-M.; Hillenkamp, J.; Bäumler, W.; Vasold, R. Light-induced decomposition of indocyanine green. *Invest. Ophthalmol. Vis. Sci.* **2008**, *49*, 1777–1783. https://doi.org/10.1167/iovs.07-0911
33. Barreto, J. C.; Smith, G. S.; Strobel, N. H.; McQuillin, P. A.; Miller, T. A. Terephthalic acid: a dosimeter for the detection of hydroxyl radicals in vitro. *Life Sci.* **1995**, *56*, 89–96. https://doi.org/10.1016/0024-3205(94)00925-2
34. Sharma, J.; Singh, R.; Singh, H.; Singh, T.; Singh, P.; Thakur, A.; Tripathi, S. K. Synthesis of $SnSe_2$ thin films by thermally induced phase transition in SnSe. *J. Alloys Comp.* **2017**, *724*, 62–66. https://doi.org/10.1016/j.jallcom.2017.06.344
35. Chen, H.; Shin, D.-W.; Nam, J.-G.; Kwon, K.-W.; Yoo, J.-B. Selenium nanowires and nanotubes synthesized via a facile template-free solution method. *Mater. Res. Bull.* **2010**, *45*, 699–704. https://doi.org/10.1016/j.materresbull.2010.02.016
36. Dieguez, A.; Romano-Rodriguez, A.; Vilà, A.; Morante, J. The complete Raman spectrum of nanometric $SnO_2$ particles. *J. Appl. Phys.* **2001**, *90*, 1550–1557. https://doi.org/10.1063/1.1385573
37. [1]Akram, M.; Wan, I.; Wan, A.; Awan, A.; Hussain, R. Continuous microwave flow synthesis (CMFS) of nano-sized tin oxide: effect of precursor concentration. *Ceram. Int.* **2016**, *42*, 8613. https://doi.org/10.1016/j.ceramint.2016.02.092
38. Malik, R.; Rana, P.; Duhan, S.; Nehra, S. One-pot hydrothermal synthesis of porous $SnO_2$ nanostructures for photocatalytic degradation of organic pollutants. *Energy Environ. Focus* **2015**, *4*, 340–345.https://doi.org/10.1166/eef.2015.1182
39. Winyayong, A.; Wongsaprom, K. Nanostructures of tin oxide by a simple chemical route: synthesis and characterization. *J. Phys.: Conf. Ser.* **2019**, *1380*, 012002. https://doi.org/10.1088/1742-6596/1380/1/012002
40. Daimon, T.; Hirakawa, T.; Nosaka, Y. Monitoring the formation and decay of singlet molecular oxygen in $TiO_2$ photocatalytic systems and the reaction with organic molecules. *Electrochemistry* **2008**, *76*, 136–139. https://doi.org/10.5796/electrochemistry.76.136
41. Tang, C. Y.; Wu, F. Y.; Yang, M. K.; Guo, Y. M.; Lu, G. H.; Yang, Y. H. A classic near-infrared probe indocyanine green for detecting singlet oxygen. *Int. J. Mol. Sci.* **2016**, *17*, 219. https://doi.org/10.3390/ijms17020219
42. Bhagwansingh, R.; Kale, R. Hydro/solvothermally synthesized visible light driven modified $SnO_2$ heterostructure as a photocatalyst for water remediation: a review. *Environ. Adv.* **2021**, *5*, 100081. https://doi.org/10.1016/j.envadv.2021.100081

 doi:10.20944/preprints202507.2363.v1




43. Carboni, D.; Marongiu, D.; Rassu, P.; Pinna, A.; Amenitsch, H.; Casula, M.; Marcelli, A.; Cibin, G.; Falcaro, P.; Malfatti, L.; Innocenzi, P. Enhanced Photocatalytic Activity in Low-Temperature Processed Titania Mesoporous Films. *J. Phys. Chem. C* **2014**, *118*, 12000–12009. https://doi.org/10.1021/jp501653x
44. Charbouillot, T.; Brigante, M.; Mailhot, G.; Maddigapu, P. R.; Minero, C.; Vione, D. Performance and selectivity of the terephthalic acid probe for OH as a function of temperature, pH and composition of atmospherically relevant aqueous media. *J. Photochem. Photobiol. A Chem.* **2011**, *222*, 70–76. https://doi.org/10.1016/j.jphotochem.2011.05.003
45. Lesniewicz, A.; Lewandowska-Andralojc, A. Probing mechanism of Rhodamine B decolorization under homogeneous conditions via pH-controlled photocatalysis with anionic porphyrin. *Sci. Rep.* **2024**, *14*, 22600. https://doi.org/10.1038/s41598-024-73586-3
46. Franchi, D.; Zacharias, A. Applications of sensitized semiconductors as heterogeneous visible-light photocatalysts in organic synthesis. *ACS Sustain. Chem. Eng.* **2020**, *8*, 15405–15429. https://doi.org/10.1021/acssuschemeng.0c05179